Three-Dimensional Printing of High-Content Graphene Scaffolds for Electronic and Biomedical Applications

Adam E. Jakus,[†,§] Ethan B. Secor,[†] Alexandra L. Rutz,[‡,§] Sumanas W. Jordan,[⊥] Mark C. Hersam,[*,†,∥] and Ramille N. Shah[*,†,§,⊥]

[†]Department of Materials Science and Engineering, Northwestern University, 2220 Campus Drive, Evanston, Illinois 60208, United States, [‡]Department of Biomedical Engineering, Northwestern University, 2145 Sheridan Road, Evanston, Illinois 60208, United States, [§]Simpson Querrey Institute for BioNanotechnology, Northwestern University, 303 East Superior Street, Chicago, Illinois 60611, United States, [⊥]Department of Surgery, Northwestern University, 251 East Huron Street, Galter 3-150, Illinois 60611, United States, and [∥]Department of Chemistry, Northwestern University, 2220 Campus Drive, Evanston Illinois 60208, United States

ABSTRACT The exceptional properties of graphene enable applications in electronics, optoelectronics, energy storage, and structural composites. Here we demonstrate a 3D printable graphene (3DG) composite consisting of majority graphene and minority polylactide-*co*-glycolide, a biocompatible elastomer, 3D-printed from a liquid ink. This ink can be utilized under ambient conditions *via* extrusion-based 3D printing to create graphene structures with features as small as 100 μm composed of as few as two layers (<300 μm thick object) or many hundreds of layers (>10 cm thick object). The resulting 3DG material is mechanically robust and flexible while retaining electrical conductivities greater than 800 S/m, an order of magnitude increase over previously reported 3D-printed carbon materials. *In vitro* experiments in simple growth medium, in the absence of neurogenic stimuli, reveal that 3DG supports human mesenchymal stem cell (hMSC) adhesion, viability, proliferation, and neurogenic differentiation with significant upregulation of glial and neuronal genes. This coincides with hMSCs adopting highly elongated morphologies with features similar to axons and presynaptic terminals. *In vivo* experiments indicate that 3DG has promising biocompatibility over the course of at least 30 days. Surgical tests using a human cadaver nerve model also illustrate that 3DG has exceptional handling characteristics and can be intraoperatively manipulated and applied to fine surgical procedures. With this unique set of properties, combined with ease of fabrication, 3DG could be applied toward the design and fabrication of a wide range of functional electronic, biological, and bioelectronic medical and nonmedical devices.

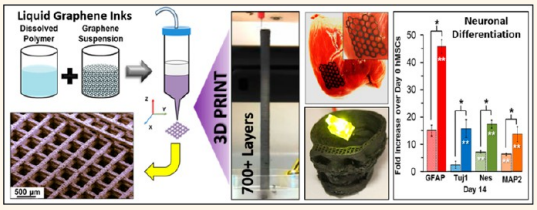

KEYWORDS: graphene · 3D printing · tissue engineering · neurogenesis

Graphene has been the focus of significant interest in both academic and industrial settings.[1] With exceptional electronic,[2] mechanical,[3] and thermal[4] properties, it is widely hailed for a range of applications from high-speed electronics[5] and energy storage devices[6] to electrochemical sensors.[7,8] More recently, it has been used as a new biocompatible, conductive biomaterial[9,10] for drug delivery,[11] stem cell differentiation,[12] biosensors,[13] imaging,[14] and osteo, cardiac, and neuro tissue engineering and regeneration.[15−18] The direct manipulation of graphene, on micro- and macroscopic scales, is desirable for many of these applications. In this regard, digital, additive, and solution-phase printing technologies offer a promising approach. For example, inkjet and gravure printing of graphene have been demonstrated for a range of devices including transistors, supercapacitors, transparent conductors, and interconnects.[7,19−24] While significant and having many applications, demonstrations to date remain limited to thin film, paper, or hydrogel composite formats.[7,11,23−27] Here we extend the fabrication of graphene structures to the third dimension using three-dimensional (3D) printing to greatly expand the versatility and functionality of this material for emerging electronic and biomedical applications.

3D printing is widely considered a revolutionary manufacturing technology, with significant promise in a broad range of fields including tissue and organ engineering. Direct ink writing is an extrusion-based 3D printing technique involving the deposition of a liquid material ink that rapidly solidifies upon extrusion and allows the fabrication of 3D objects layer-by-layer. Direct ink writing is also compatible with multimaterial

* Address correspondence to ramille-shah@northwestern.edu, m-hersam@northwestern.edu.

Received for review February 20, 2015 and accepted April 10, 2015.

Published online April 10, 2015
10.1021/acsnano.5b01179

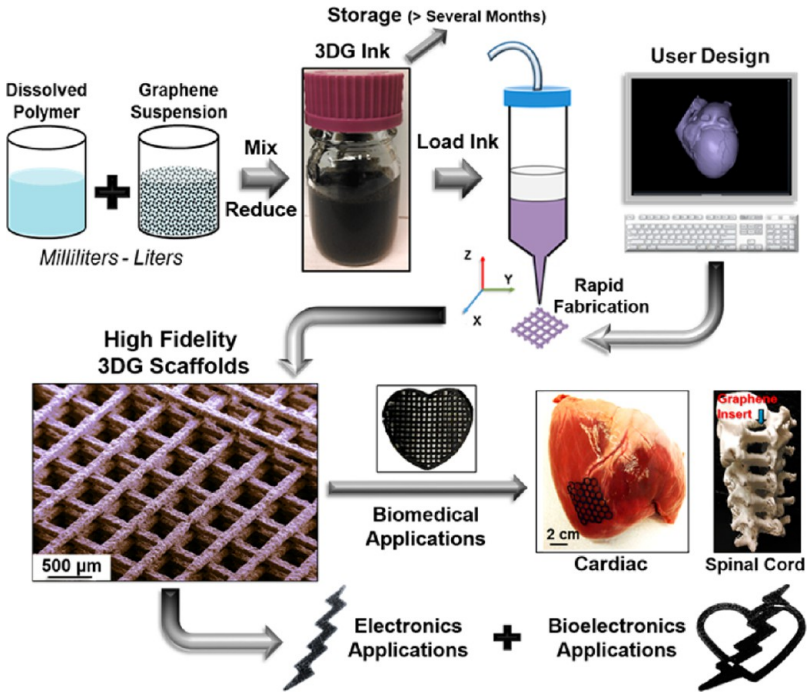

Figure 1. 3DG inks are produced through simple combination and mixing of the elastomer solution with the dispersion of graphene powder in a graded solvent followed by volume reduction and thickening, a process that can be scaled up to many liters at once if desired. User-defined architectures 3D-printed from 3DG have a variety of potential applications, including those relating to energy storage and bioelectronics, as well as tissue and organ engineering.

printing, offering a distinct advantage for integrating multiple functionalities in a 3D printing format. Further development of materials compatible with 3D printing will continue to expand its scope and impact.[28,29] While carbon-composite inks have been previously developed for 3D printing applications,[30,31] graphene-based inks offer enhanced functionality and improved electrical, mechanical, and biological properties.

In light of this, we present here the development and use of 3D printable graphene inks that result in electrically conductive, mechanically resilient, and biocompatible scaffolds with high graphene content (60 vol % of solid). This solvent-based 3D graphene (3DG) ink comprises graphene flakes and the biocompatible, biodegradable, and hyperelastic polyester polylactide-*co*-glycolide (PLG). Although PLG is widely used in biomaterials research, it has not been previously utilized as a binder in combination with a mixture of graded volatility solvents. 3DG can be printed at room temperature *via* extrusion into self-supporting, user-defined structures with fidelity and precision. The resulting majority graphene structures are mechanically robust and plastic in nature, with thin constructs displaying a high degree of flexibility. Furthermore, the 3DG presented here exhibits improved electrical conductivity compared to previously reported 3D-printed carbon-based materials.[30,31] We explore the potential use of these constructs as electrically conducting scaffolds primarily for tissue regenerative engineering applications using *in vitro* and *in vivo* biocompatibility studies. Overall, this 3DG ink enables rapid fabrication of 3D graphene objects with novel and desirable mechanical, electrical, biological, and handling properties. Additionally, simple and scalable ink preparation, along with room temperature 3D printing, enables versatile design and fabrication of graphene objects with additional potential applications in medicine, bioelectronics, sensors, and energy devices (Figure 1).

RESULTS AND DISCUSSION

3DG Ink Synthesis and 3D Printing. The 3DG ink presented in this study was prepared from commercially available materials using standard mixing of components followed by solvent evaporation, all performed under ambient conditions. The ease of preparation of this ink and its long shelf life of at least several months render it a highly scalable procedure. To prepare the graphene-based inks, PLG is first dissolved in dichloromethane (DCM), a high vapor pressure solvent. Separately, graphene powder [3−8 atomic layers thick, 3:2 (60 vol % or ~75 wt % graphene; 3DG), 2:3 (40 vol % or ~56 wt % graphene), and 1:4 (20 vol % or ~32 wt % graphene) by volume graphene:PLG, corresponding to approximately 3:1, 3:2, and 3:7 by weight, respectively] is dispersed in a mixture of DCM and smaller relative volumes of 2-butoxyethanol, a common surfactant, and dibutyl phthalate, an effective plasticizer, a solvent system that has previously been used for printing particle-laden inks.[32] DCM is initially added in excess

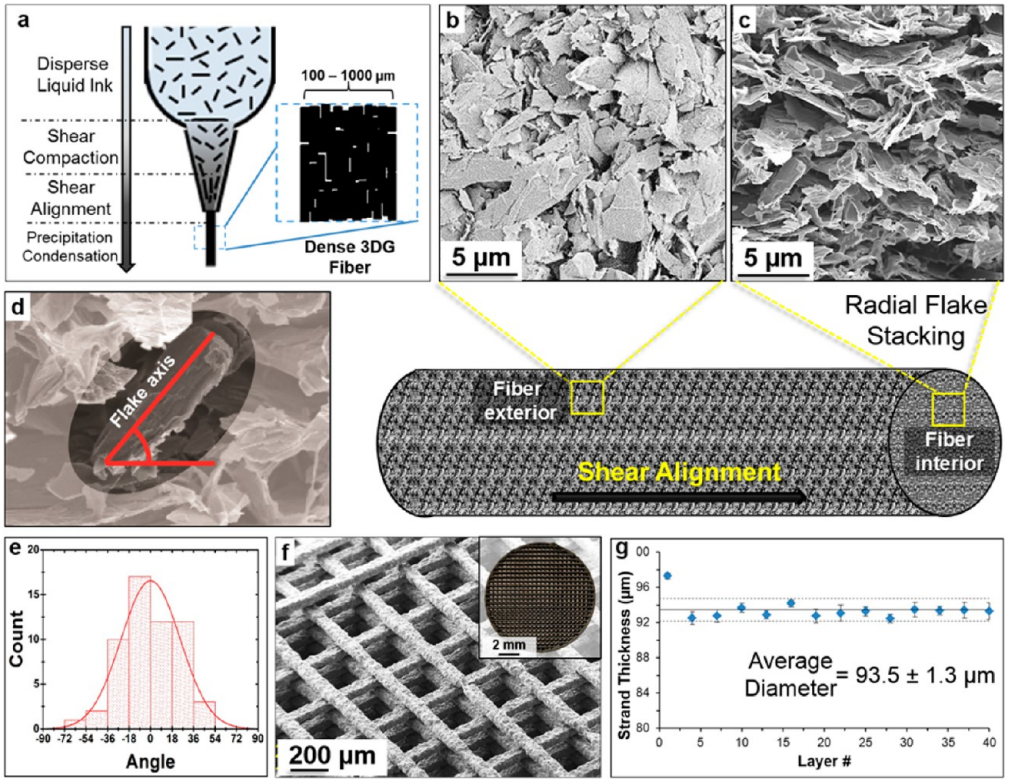

Figure 2. (a) 3DG (60% by volume graphene, 40% PLG) inks are liquid prior to extrusion. Upon application of pressure and flow into the narrowing diameter nozzle, shear forces result in graphene flake alignment. Upon exiting the nozzle, DCM rapidly evaporates, solidifying the fiber and resulting in a slight diameter reduction. (b,c) Scanning electron microscopy (SEM) images of the fiber exterior and cross section, respectively, reveal that this process results in flake alignment along the exterior of the fibers and flake stacking within the fibers. (d) Example illustrating the measurement of flake orientation in an end-on cross sectional view of the 3DG fiber. (e) Histogram of graphene flake orientations with respect to the horizontal. The distribution around 0° indicates that there is a preferential alignment of the flakes within the fiber interior. (f) SEM and optical (inset) images of 3DG structures printed with a 100 μm tip, displaying a high degree of regularity. (g) Uniformity of 3DG structure quantified by fiber thickness in a 40 layer construct printed with a 100 μm tip. While the first layer deviates from the mean due to spreading on the substrate, the subsequent 39 layers show narrow standard deviations within particular layers (error bars on individual points) as well across many layers (dashed bounding lines on either side of the solid, mean line), with average diameter and deviation given.

to permit easy mixing and dispersion of components. The PLG solution and graphene dispersion are combined and thoroughly mixed by hand, vortexing, or rocking until homogeneous. Over the course of several hours (dependent on total ink volume), excess DCM evaporates while open in a sonicating bath until a quasi-static shear rate viscosity of approximately 30 Pa·s is achieved. At this point, the 3DG ink may be stored in a well-sealed glass container under refrigeration prior to use. The shear-thinning nature of the ink, combined with the graded volatility of the solvents, allows for room temperature extrusion-based printing to produce self-supporting structures (Supporting Information Figure S1a).

When printing 3DG, which is composed of 60 vol % graphene and 40 vol % PLG (corresponding to 75 wt % graphene, 25 wt % PLG), the 2D nature of the graphene particles and the uniaxial nature of the printing process couple to produce objects with anisotropic microstructure and properties. The 3DG ink is a relatively viscous dispersion of randomly oriented graphene particles suspended in a dissolved elastomer solution. Upon extrusion (Figure 2a), resulting shear forces promote reorientation and alignment of the flakes along the direction of flow. The net effect is a filament microstructure with flakes oriented along the fiber surface (Figure 2b–e). This is distinct from samples cast from the ink, which exhibit more random orientation (Figure S1b). The elastomer is present in sufficient quantities to form a continuous, interconnecting matrix between the graphene flakes (Figure S1b). Rapid evaporation of the DCM solvent following extrusion is critical to create self-supporting fibers that do not significantly deform following deposition (Figure 2a). Under ambient conditions, DCM has a vapor pressure exceeding 50 kPa, roughly nine times that of pure ethanol under the same conditions (5.5 kPa). The high vapor pressure of DCM, combined with the high surface area to volume ratio of extruded material, results in rapid evaporation of DCM, producing self-supporting fibers upon extrusion. The presence of the remaining low vapor pressure solvents, 2-butoxyethanol (0.1 kPa) and dibutyl phthalate (9×10^{-6} kPa), imparts enough liquidity to the deposited material to enable seamless merging of subsequent

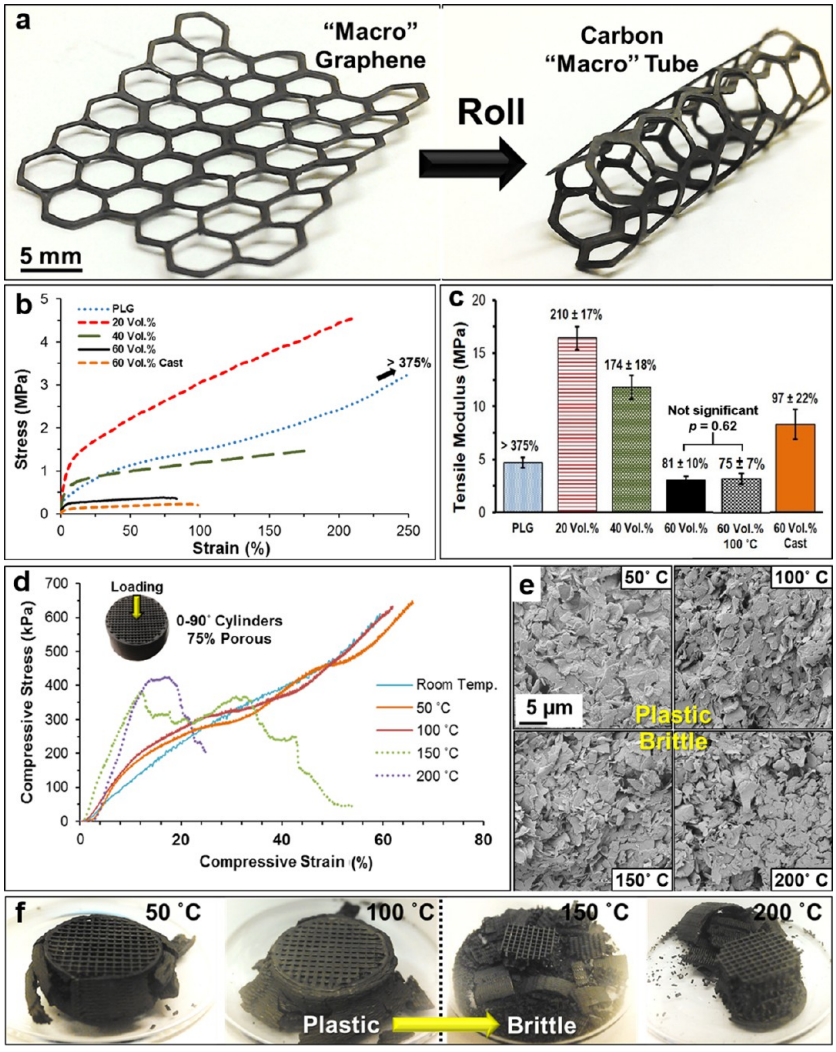

Figure 3. (a) Photographs depicting that thin 3DG sheets are flexible and can be rolled into more complex 3D forms that may be difficult to 3D-print directly. (b) Quasi-static tensile measurements of pure 3D-printed PLG, 3D-printed PLG–graphene composites, and cast 60 vol % graphene composite. (c) Corresponding elastic moduli obtained from tensile results and average percent strain-to-failure for each sample group (n = 4), which includes as-printed 60 vol % graphene (3DG), 100 °C annealed for 30 min 3DG, and cast 60 vol % ink. All groups' moduli and strain-to-failure are significantly different from each other ($p \ll 0.05$) except for 60 vol % and 60 vol % 100 °C. (d) Compression measurement of 75% porous 3DG (60 vol %) cylinders following annealing at multiple temperatures, illustrating characteristic ductile-to-brittle transition between 100 and 150 °C. (e) SEM micrographs of thermally treated 60 vol % graphene samples, indicating that the particle network does not vary significantly as a function of temperature. (f) Optical images of 60 vol % cylinders following compression testing, illustrating the brittle failure resulting from annealing above 150 °C.

3D-printed layers (Supporting Information videos 1 and 2), resulting in physically smooth transitions between adjacent layers, a common challenge for direct ink write 3D printing technologies. The result of this process is a 3DG ink that can be extruded from tip diameters as small as 100 μm and at speeds greater than 40 mm/s to produce highly uniform, multilayered structures (Figure 2f). Detailed characterization reveals that individual strands comprising the structure are approximately 6% smaller than the tip diameter, providing evidence of volume reduction during drying. In addition, the dimensions of printed fibers are consistent both within a single layer and across dozens of layers, with an average strand thickness among 120 measured strands deviating only 1.4% from the mean (Figure 2g).

Characterization of Mechanical Properties. Despite its high particle content, the graphene–polymer composite is mechanically stable and versatile. The unique properties of 3DG enable thinner printed structures (Supporting Information video 3) to be rolled, folded, cut, and even fused together using 3DG ink. In this manner, a complex 2D geometric hexagonal array can be rolled by hand to form a 3D object, such as a carbon "macrotube" (Figure 3a). The flexible nature of these printed objects is attributed to the specific choice of PLG as the polymer binder. To more quantitatively assess the mechanical behavior of the 3DG system and composites with lower graphene loading, tensile and compressive properties of the 3D-printed constructs were tested. Although not nearly as elastic as their pure

PLG counterpart, 3D-printed graphene–PLG composites can be strained to greater than 210% for 20 vol % (of solid) graphene loading and 81% for 60 vol % graphene loading prior to failure (Figure 3b). As expected, strain-to-failure is inversely proportional to graphene loading. However, the elastic modulus, although initially increased over pure PLG for 20 vol % graphene, decreases significantly with increased graphene content (Figure 3c), ultimately resulting in a modulus of 3 MPa for 3DG (60 vol % graphene). We believe that this is due to the fact that tensile loads are primarily carried by the PLG elastomer. As graphene content increases toward and beyond 40 vol %, PLG is unable to sufficiently coat and tightly bond neighboring graphene particles, decreasing both the strength and elastic moduli of the high graphene content composites. We note that cast 60 vol % graphene samples were approximately three times stiffer than their 3DG counterparts (Figure 3c). We believe this variance stems from differences in flake orientation and material porosity. Because they can slip past each other, aligned flakes in the 3D-printed constructs require less force to translate along a parallel direction of loading. In the cast system, flakes are more randomly oriented (Figure S1b) in a manner that inhibits slip upon loading, resulting in an increased elastic modulus. Interestingly, the shape of the graphene flakes contributes significantly to the stability and flexibility of the resulting 3D-printed structures. Other carbon-based nanoparticles, such as aggregated carbon nanotubes formed into inks and printed in the same manner as 3DG, result in structures that are exceptionally brittle and fracture after minimal handling (Figure S2). In this latter case, the dense, micron-scale clusters of carbon nanotubes cannot translate upon loading, resulting in brittle fracture. Under compressive loads, 3DG cylinders display typical plastic foam behavior (Figure 3d). These tensile and compressive properties are maintained even when samples are annealed in air up to 100 °C but deteriorate rapidly at temperatures equal to or exceeding 150 °C (Figure 3d) due to PLG decomposition. Although inspection of the various microstructures (Figure 3e) does not reveal a significant variation between samples annealed at the different temperatures, structures heated above 150 °C undergo brittle failure upon compression (Figure 3f).

Characterization of Electrical Properties. Due to the widespread application of graphene in electronic and electrochemical devices, we characterized the electrical properties of the 3D-printed graphene fibers and constructs. Open-mesh cylinders fabricated from 3DG support the electrical current as-printed, as illustrated by an activated light-emitting diode (LED) in series with the 3DG cylinders (Figure 4a). Resistivity measurements of as-printed 3DG fibers verify their electrical conductivity (Figure 4b). Annealing in air up to 500 °C leads to no noticeable volume change in fibers or 3D-printed porous cylinders (Figure S3a); however, the resistivity measured along the fiber length decreases to $0.114 \pm 0.002\ \Omega\cdot$cm (conductivity of approximately 875 S/m) when structures are annealed in air at 100 °C. This resistivity represents an order of magnitude improvement over previously reported carbon-based 3D conductive inks.[30,31] The conductivity of 3DG along the fiber direction is inversely dependent on the diameter of the extrusion tip, with small-diameter (<400 μm) extrusion tips corresponding to lower resistivity (Figure 4c). This difference is likely associated with the microstructure of the extruded filament. Fibers extruded from small-diameter tips experience a higher shear rate during extrusion, facilitating more complete alignment of the graphene flakes. Additionally, small-diameter fibers exhibit a higher surface-to-bulk ratio, enhancing the effect of particle alignment at the surface. The filament resistance scales with the cross sectional area (Figure S3b) according to a power-law relationship having an exponent of -0.79 ± 0.03, which is intermediate between bulk and surface conduction exponents of -1 and -0.5, respectively (Figure S3c), indicating enhanced electrical conductivity along the surface. This corresponds well with the description of shear-induced flake alignment, as well as previously reported electrical effects of graphene alignment,[33] as the shear rate is significantly higher at the fiber surface due to the confined flow geometry and the shear-thinning nature of the ink. In general, the shear alignment of graphene flakes during extrusion, supported by both morphological and electrical characterization, offers a compelling foundation for the alignment of other anisotropic nanomaterials to more precisely tailor the properties of 3D-printed objects.

The electrical properties of the material are also dependent on graphene loading (Figure 4d). Even a lower loading of 20 vol % graphene results in appreciable conductivity. While exhibiting a lower electrical conductivity, these lower graphene content composites are significantly stiffer and can undergo three times more strain prior to failure than the 3D-printed 60 vol % graphene composites (Figure 3b,c). This range of mechanical and electrical properties indicates the potential to tailor the 3D-printed graphene system to specific applications by simply altering the particle content in the initial inks.

Because 3DG exhibits flexibility and mechanical tolerance, its electrical properties under mechanical deformation were also evaluated. Resistance increases by a factor of approximately 10 for 400 μm fibers strained up to 20% (Figure 4e), likely resulting from the reduced points of contact between individual graphene particles as the elastomer is strained around them. In contrast, under cyclic loading to small strains (experienced during bending), the conductivity is maintained, indicating the reversibility of the deformation.

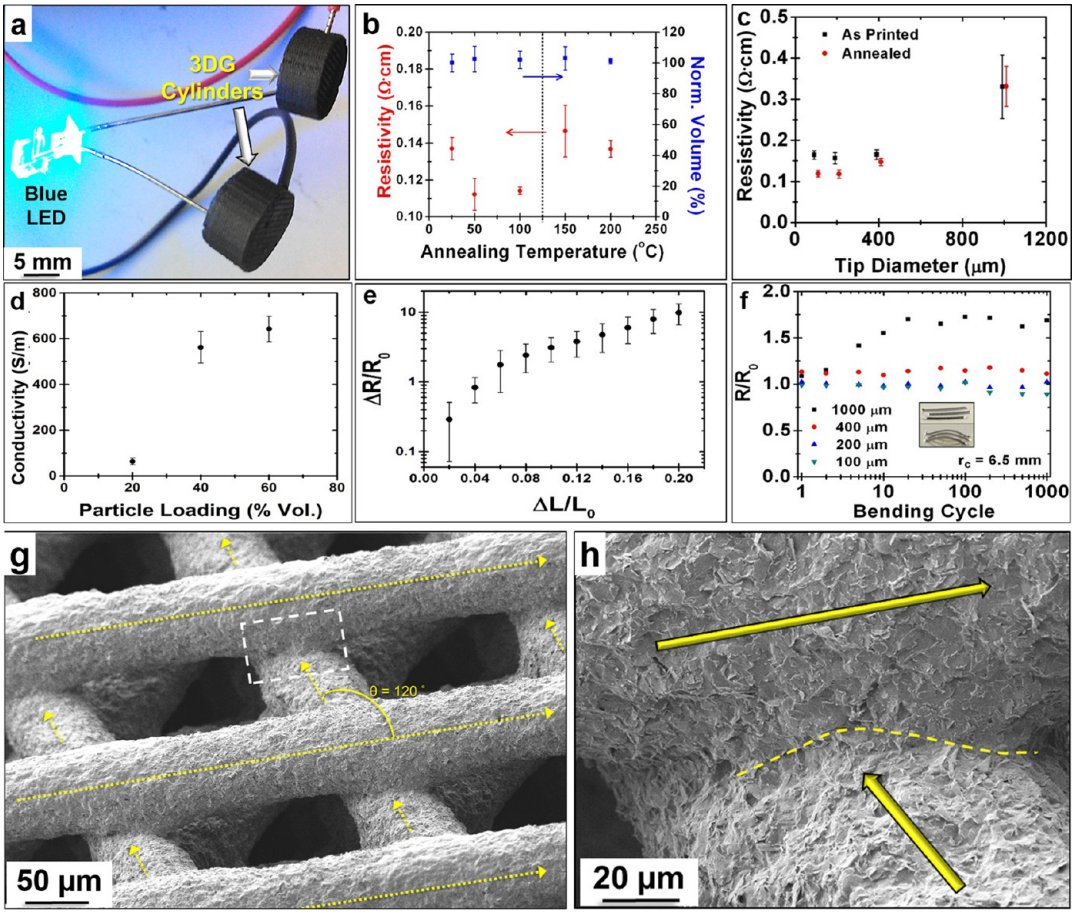

Figure 4. (a) Demonstration of electrical conductivity of objects as-printed, showing two 3DG cylinders incorporated into a circuit with a blue LED. (b) Resistivity and normalized volume of 200 μm printed 3DG fibers as a function of annealing temperature (dotted vertical line represents boundary between plastic and brittle behavior). (c) Resistivity of graphene fibers along the fiber direction for various diameter extrusion tips, before and after annealing at 100 °C for 30 min in air; the observed diameter-dependent resistivity may be correlated with increased flake alignment for small-diameter extrusion tips. (d) Conductivity of non-annealed fiber extruded from a 400 μm diameter tip, measured along fiber direction, as a function of graphene loading. (e) Electrical resistance of a 400 μm diameter 3DG fiber as a function of tensile strain. As the fiber is strained, resistance increases. This is likely due to increased spatial separation and reduced contact of graphene flakes within the composite, disrupting the continuous graphene network. (f) Resistance of printed graphene fibers on a PEN substrate over 1000 bending cycles to a radius of curvature of 6.5 mm, showing an irreversible resistance increase for large-diameter fibers corresponding to buckling deformation with inset images of large-diameter graphene fibers prior to bending and following 1000 bending cycles. (g,h) SEM micrographs of fiber−fiber junctions 3D-printed with a 100 μm diameter tip, showing seamless transition between adjacent 3D-printed layers (yellow dotted line in h). Arrows indicate fiber directions. Error bars represent a standard deviation of measurements for 3−7 samples in each case.

3DG filaments were printed onto a 50 μm thick polyethylene naphthalate (PEN) film for handling. Figure 4f presents the evolution of the line resistance for fibers of 100, 200, 400, and 1000 μm tip diameter over 1000 bending cycles to a radius of curvature of 6.5 mm. In this measurement design, the entire fiber is under tension during flexing. While the small-diameter fibers exhibit little variation in resistance, the large-diameter fibers undergo an irreversible deformation (Figure 4f, lower inset), which corresponds to an increase in resistance by a factor of 1.68 $\pm$ 0.04. This ability for small-diameter fibers to maintain mechanical integrity and electrical conductivity through many bending cycles is beneficial for *in vivo* tissue engineering applications where natural internal and external movement of the body are likely to place mechanical strain on the implanted objects.

While the results thus far correspond to single printed fibers, with resistance measurements taken along the printing direction, 3D-printed structures contain networks of connected fibers. In such complex structures, the junctions between fibers can dominate the electrical properties of the system. As shown in Figure 4g,h, the junctions between two subsequent layers of graphene are characterized by smooth, seamless transitions due to the solvent evaporation dynamics of the system (Supporting Information video 1), which enable adjacent layers to seamlessly fuse together while retaining their structural integrity. Measurements of the absolute resistance associated with this junction indicate a value below the measurement variability of approximately 10 Ω, indicating excellent layer-to-layer fusion.

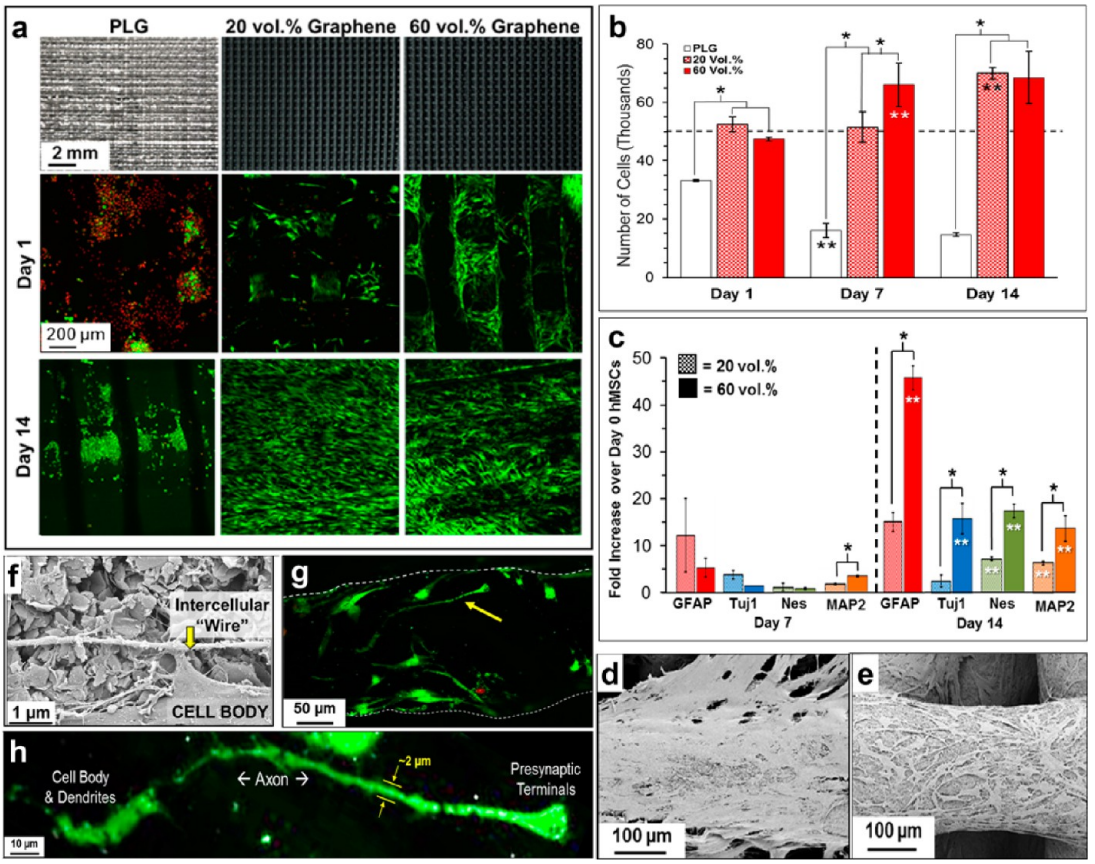

Figure 5. (a) Photographs (top row) and scanning laser confocal 3D reconstruction projections of live stained (green) and dead stained (red) hMSCs on various scaffolds 1, 7, and 14 days after being seeded. (b) Number of hMSCs present on scaffolds (n = 3) as a function of material and days after seeding as determined from DNA quantification. Dotted line represents initial cell seeding number (50 000). (c) Neurogenic relevant gene expression of cells on 20 and 60 vol % graphene 7 and 14 days after being seeded normalized to expression of day 0, unseeded hMSCs. SEM micrographs of hMSCs on (d) 20 and (e) 60 vol % graphene scaffolds 7 days after being seeded. (f) Higher-magnification SEM micrograph of cells on day 7, 60 vol % graphene scaffolds, showing hMSC connecting *via* a small segment of a long, "intercellular" wire. (g) Scanning laser confocal 3D reconstruction of live (green) and dead (red) cells on day 14 for 60 vol % graphene scaffolds and (h) detail of cell indicated by yellow arrow in (f). For panels b and c, * indicates significance of $p < 0.05$ between compared groups (n = 4); ** indicates significant ($p < 0.05$) difference over previous time point for the same material group.

***In Vitro* Biocompatibility and Bioactivity.** Graphene has received considerable interest as a promising new biomaterial in recent years.[9,10] Although its long-term biocompatibility has yet to be fully evaluated,[34,35] it is one of few potentially biocompatible materials that exhibits electrical conductivity, a characteristic shown to enhance cell−cell signaling, cell differentiation, and cell function in a variety of cell types, including those comprising muscle, cardiac, and nervous tissues.[16−18,36] 3DG presents an optimal graphene system for biological applications because (1) it comprises PLG, a widely used biomedical polymer that is also biodegradable,[37] (2) it is flexible and has an intrinsic elastic modulus (3.0 ± 0.4 MPa) similar to that of soft tissues, such as spinal cord (1−2.3 MPa),[38−40] and (3) porosity of the 3D-printed objects can be designed and tailored to optimize cell response and tissue integration for specific applications. To determine if 3DG can support cell viability and proliferation, and whether or not it can influence stem cell fate, female bone-marrow-derived human mesenchymal stem cells (hMSCs) were statically seeded onto 4 mm diameter 3D-printed scaffolds containing 60 vol % graphene (3DG) (Figure S4a), 20 vol % graphene, and pure 3D-printed PLG.

Over the course of 2 weeks, in standard Dulbecco's modified Eagle medium (DMEM), hMSCs remain viable on 20 and 60 vol % graphene scaffolds (Figure 5a) and proliferate (Figure 5b) to coat individual struts and span the interstrut gaps. Viability and proliferation on PLG using the same solvent-based room temperature printing method was significantly lower relative to that of the graphene-containing scaffolds. This difference could be due to a number of variables including surface roughness, mechanical properties, and electrical conductivity. Both 20 and 60 vol % graphene scaffolds supported hMSC viability and proliferation to a similar degree; however, significant variations in phenotypic response were observed by day 14. Glial and neurogenic relevant genes, glial fibrillary acidic protein (GFAP), neuron-specific class III β-tubulin (Tuj1), nestin (Nes), and microtubule-associated protein 2 (MAP2)

are upregulated in cells on both 20 and 60 vol % graphene scaffolds over the course of 2 weeks relative to initial expression of unseeded day 0 hMSCs (Figure 5c). By day 14, however, cells on 60 vol % graphene exhibit 6, 3, 2.5, and 2 times greater expression of GFAP, TujI, Nes, and MAP2, respectively, compared to cells on the 20 vol % graphene scaffolds. There is also a distinct difference in cell morphology at this time, where hMSCs on 20 vol % graphene exhibit a confluent sheet-like morphology (Figure 5d), which is characteristic of adherent cell types such as fibroblasts and similar hMSC lineages. In contrast, hMSCs on 60 vol % graphene develop into highly elongated morphologies and do not form confluent sheets (Figure 5e). Instead, high aspect ratio cellular extensions (often greater than 100 μm) are found throughout the 60 vol % graphene scaffolds, connecting individual cells through "wire-like" networks (Figure 5f). Closer inspection of cells on day 14 (Figure 5g) illustrate that a segment of the population exhibits morphologies similar to uni- or multipolar neurons,[41] including approximately 2 μm diameter axon-like extensions, consistent with those of unmyelinated axons[42] as well as features that resemble presynaptic terminals (Figure 5h).

While there is ample evidence that neuronal stem cell function and differentiation can be aided in the presence of graphene and graphene-oxide-modified substrates and foams,[20,43−45] there is less work illustrating that hMSCs cultured under similar conditions, in the presence of graphene, can differentiate and become neuron-like.[46] The few existing studies that do demonstrate this potential, however, show that hMSC differentiation into neuron-like cells is possible when cultured in media containing neuronal-inducing chemical and biological factors, such as retinoic acid,[46] bFGF, and BDNF.[41] We show here, however, that with elevated graphene concentrations presented by 3DG, exogenous factors may not be required to induce neurogenic differentiation of hMSCs, demonstrating its inherent neuronal-inducing capabilities. These results show great promise in using 3DG scaffolds as conducting microenvironments for stem cell differentiation. More in-depth future experiments will need to be performed to identify the exact mechanisms by which 3DG affects cellular differentiation and neurogenic function. In addition to hMSCs, cardiomyocytes and human neurons derived from induced pluripotent stem cells have also been cultured within 3DG and successfully adhere to and survive within these high graphene content constructs (Figure S4c). These results demonstrate the potential of 3DG as a new conducting scaffold for electrogenic tissue regeneration.

***In Vivo* Biocompatibility.** *In vivo* biocompatibility of 3DG was also evaluated in a mouse subcutaneous implant model (Figure S2a). Control PLG and 3DG samples were extracted 7 and 30 days after initial implantation for histological, immunohistochemical, and SEM observations. After 7 days *in vivo* (Figure S5b), there is no indication of a severe immune response or fibrous capsule formation around individual 3DG struts or the scaffold as a whole. At this time point, a significant amount of web-like extracellular matrix (ECM) with concentric circular morphologies, composed primarily of collagen, was observed within the pores of the scaffold (Figure 6a−c). SEM revealed a tissue matrix with distinct porous architectures within the 3DG (Figure 6i and Supporting Information Figure S5c−e) that are not observed in the PLG control (Figure S6d−f). By day 7, cells are beginning to physically break down the 3DG around the outer edges of the scaffold (Figure 6d). Day 7 samples stained negative for inflammatory factor COX-2 as well as macrophages (Figure S7), further validating biocompatibility at this early time point. After 30 days *in vivo*, host tissue is fully integrated within the 3DG scaffolds (Figure 6e and Figure S5a), and significant deformation of the 3DG structure is apparent. This is expected due to the relatively soft and flexible nature of 3DG within a fully integrated, dynamic environment, such as a subcutaneous pocket. Similar to day 7, the majority of ECM within the scaffold interior is collagen (Figure 6g). A major difference, however, is that by day 30 the ECM is considerably both more dense than day 7 and heavily vascularized, with large vessels, as well as many single-cell capillaries (Figure 6h,j and Figure S5f−i). Furthermore, after 30 days, large numbers of cells are localized around the 3DG struts (Figure 6g and Figure S5j,k), and there is still no evidence of fibrous capsule (*i.e.*, dense acellular region of ECM) formation surrounding the material. These cells are confirmed to be primarily macrophages (Figure S7) and appear to be breaking down the 3DG scaffold by physically removing individual graphene flakes and small aggregates. Gross histological analyses of the kidneys, livers, and spleens (Figure S8) removed from mice after 30 days of 3DG and PLG scaffold implantation did not reveal the presence of any graphene flakes. This indicates that either the graphene flakes were cleared from these organs or the graphene flakes remain in close proximity to the original implantation site after being dissociated from the main scaffold structure by macrophages. Due to the relatively large size of the graphene flakes (micron-scale), it is unlikely that they would be cleared from these organs and, more likely, that they predominantly remained near the initial implant site, embedded in the surrounding tissues.

3DG biodegradability primarily depends on the hydrolysis of the PLG component of the 3DG scaffold into lactic and glycolic acids.[37] Graphene particles are not biochemically degradable; however, it is apparent that flakes are small enough to be physically manipulated and relocated by cells (Figure S5i,j). Although further studies are required to determine the final,

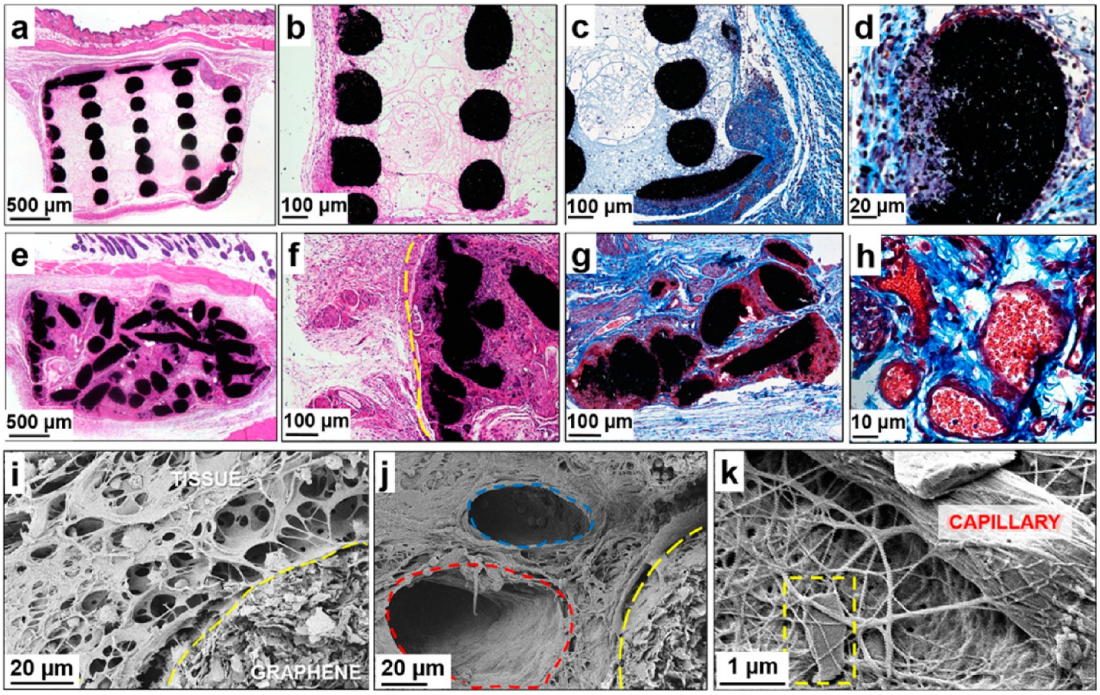

Figure 6. (a,b) Cross sectional histological images of hematoxylin and eosin (H&E) stained 3DG scaffold section explanted 7 days after initial implantation, in which pink stains indicate cellular membranes and tissue, blue stains show cell nuclei, and black is 3DG. The interior of 3DG scaffolds remains mostly acellular, but a characteristic ECM web is pervasive. (c) Masson's trichrome (MT) stained histological image of explanted 3DG scaffolds 7 days after initial implantation showing that synthesized ECM within 3DG scaffold is primarily comprised of collagen. Blue stains for collagen; red for cellular material. (d) MT stained image showing cells deconstructing 3DG strut toward the exterior of the scaffold 7 days after implantation. (e,f) H&E stained images of 3DG scaffold section 30 days after initial implantation, illustrating comprehensive integration of host tissue with 3DG scaffold. 3DG is also significantly deformed and beginning to degrade at this time. (g) MT histological image of day 30 sample illustrating that the majority of ECM is collagen with high concentrations of cells radially surrounding 3DG material. (h) MT histological image of day 30 sample showing pervasive vascularization (yellow arrows and yellow dashed lines), comprehensive collagen network, and cellular organization near 3DG material (green dotted line). (i) SEM micrograph illustrating ECM network near 3DG (bounded by yellow dotted line) 7 days after initial implantation. (j) SEM micrograph showing vessel−vein pair near 3DG 30 days after implantation. (k) SEM micrograph of graphene flake (yellow box) found embedded in the ECM matrix far from 3DG struts.

systemic destination of these graphene particles, individual particles can be observed scattered throughout and embedded within the ECM, often far from individual 3DG struts (Figure 6k). These initial *in vivo* results indicate that 3DG does not elicit an inflammatory response or fibrous encapsulation at short or extended time points and, by day 30, is actively degraded by cells—an advantageous characteristic for tissue engineering and regeneration applications where the scaffolds must break down in order to be gradually replaced by natural host tissue.

Surgical Handling of 3D-Printed Graphene. Major characteristics that are often overlooked when developing new biomaterials are surgical handling and ability to intraoperatively manipulate and form the implant to accommodate the situation. This includes being able to precisely attach the implant material, through suturing or some other means, to surrounding tissue in addition to being able to remove excess implant material from the surgical site. As a demonstration of the ability to surgically implement 3DG in clinically relevant scales, uni- (Figure 7a,b) and multichannel (Figure 7c−e) nerve conduits, similar in architecture to those described previously,[47,48] were 3D-printed. In addition to being able to produce relevant length 3DG nerve conduits of varying diameter (Figure 7b), the characteristics of the ink permits rapid fabrication of high aspect ratio objects composed of many hundreds of layers (Figure 7f and Supporting Information video 4). A large stock 3DG object such as this can be sectioned to size depending on the surgical need. In this instance, a 2 cm long section was cut from the 12 cm cylinder and sutured around and to the dorsal branch of the ulnar nerve in an unfixed human cadaver through multiple surgical steps that took advantage of the 3DG's handling physical and mechanical characteristics (Figure 7g). After the ulnar nerve was exposed, the 2 cm section of tubular 3DG nerve conduit was longitudinally cut with surgical shears, permitting it to be wrapped around the nerve bundle. After wrapping, the longitudinal 3DG cut was sutured shut along the length of the nerve conduit. Additional sutures were used to attach the 3DG nerve conduit to the surrounding epinerium and nerve bundle (Figure 7g detail). Excess conduit length was then removed using surgical shears. This procedure, although performed on a

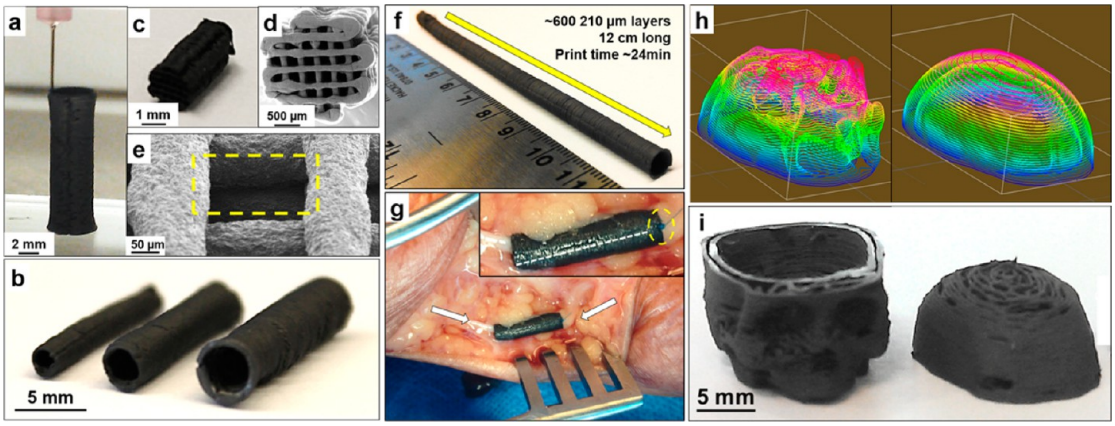

Figure 7. (a) 3DG (60 vol % graphene) ink can be rapidly 3D-printed into self-supporting tubular structures (140 layers) of (b) various sizes that could serve as custom-sized nerve graft conduits.[48] (c,d) Uniaxial, multichannel nerve guides, with very similar architectures to those reported previously,[47] may also be 3D-printed from 3DG inks. Uniaxial channels are achieved by significantly reducing the *z*-spacing of progressive layers. (e) SEM micrograph of multichannel 3DG nerve conduit with every other layer close to contact (yellow box), minimizing or eliminating pores orthogonal to the major axis of nerve guide. (f) 3DG can be 3D-printed into structures composed of many hundreds of layers, such as this high aspect ratio (24:1) 5 mm diameter hollow tube, which can be cut to size as needed. (g) Photograph of tubular 3DG nerve conduit cut from (f) that was implanted into a human cadaver *via* longitudinal transection and wrapping around the ulnar nerve (white arrows). The 3DG nerve conduit was then sutured closed along the previously described longitudinal transection (white dotted line) as well as to the surrounding epinerium and nerve tissue (inset, yellow circle). Excess 3DG nerve conduit length was then cut with surgical shears to expose additional nerve tissue. (h) Digitally sliced STL file of skull and skull cap and (i) photograph of resulting 3D-printed 3DG skull and skull cap.

cadaver, illustrates that 3DG's mechanical properties are highly advantageous for pre- and intraoperative precision surgical procedures on scales relevant to humans.

CONCLUSIONS

Using a solution-based, scalable ink, graphene can be 3D-printed under ambient conditions into arbitrarily shaped scaffolds with filaments ranging in diameter from 100 to 1000 μm. Although we primarily focus on simple architectures in this work for the purposes of material and biological characterization and evaluation, much more complex structures can be 3D-printed with ease (Figure 7h,i), elevating this 3DG ink above many other direct ink write systems that are only capable of producing simple structures comprising a maximum of several layers. This particular composite system, with a tunable graphene composition, has unique mechanical, electrical, biological, and surgical handling properties. Not only does 3DG display the highest electrical conductivity of any carbon-based 3D-printed material reported to date, but it is also mechanically flexible, biocompatible, neurogenically bioactive, biodegradable, and surgically friendly. These characteristics enable a range of potential applications in wearable and implantable electronics, sensors, and tissue engineering. *In vitro* studies confirmed that 3DG supports the viability of multiple, distinct cell types, including adult mesenchymal stem cells, which develop neuron-like morphological characteristics, as well as a large upregulation of glial and neuron-specific genes in the absence of exogenous neurogenic factors. This suggests that 3DG could have possible practical applications in nerve tissue engineering and regeneration as single[48] and multichannel[47] nerve guides (Figure 7). *In vivo* studies with 3D-printed graphene also suggest that it is biocompatible, with no evidence of graphene flakes collecting in the kidney, liver, or spleen. If the previous characteristics existed without the ability to be surgically handled and implemented, 3DG would primarily be relegated to being a research tool. However, we have also demonstrated that it can be cut, sutured, and manipulated intraoperatively for fine surgical procedures, such as nerve bundle wrapping. By concurrently achieving advances in electrical, mechanical, biological, and handling properties, combined with its ease of processing and fabrication into complex, user-defined structures, 3DG is poised to accelerate the development and manufacturing of emerging functional electronic and medical devices.

METHODS

Ink Preparation and 3D Printing. The 60 (3DG), 40, and 20 vol % graphene inks were synthesized by thorough mixing of polylactide-*co*-glycolide (85:15) copolymer (Boehringer Ingelheim, Germany), graphene powder (3−8 atomic layers thick, 5−20 μm long and wide; Graphene Laboratories Inc., USA), and a 10:2:1 by mass mixture of DCM (Sigma), ethylene glycol butyl ether (Sigma), and dibutyl phthalate (Sigma), where 0.6 g of dibutyl phthalate was added for every 2.2 g (1 cm^3) graphene. Graphene comprised 60 vol % of the solid additions, while PLG comprised the remaining 40 vol %. Inks were allowed to thicken to a viscosity 30−35 Pa·s, as determined through use of a Brookfield DV-E rotational shear viscometer, through evaporation under ambient conditions before 3D printing. Pure PLG inks

as well as 20 and 40 vol % graphene constructs were prepared following the same protocol.

All printed structures were fabricated using a 3D BioPlotter (EnvisionTEC GmbH, Germany). The 100, 200, 400, and 1000 μm diameter polyethylene tips (Nordson EFD, USA) were used throughout the study. All 3DG inks were 3D-printed onto a smooth, polytetrafluoroethylene-coated substrate. *X*−*Y* motion speeds ranged from 10 to 45 mm/s depending on the structure being fabricated. Objects could be removed from the substrate and handled immediately after printing. Applied printing pressure ranged from 0.5 bar for the 1000 μm diameter tip to 5 bar for the 100 μm tip. All ink synthesis and printing was performed at room temperature. All scaffolds for *in vitro* studies were created by 3D printing contoured 1.5 × 1.5 cm squares using a 200 μm tip; 10 layers (180 μm/layer), 200 μm spacing between deposited fibers, 0−90° fiber orientation with every other layer being offset 300 μm in *X* and *Y* relative to two layers prior. Four millimeter biopsy punches were used to "punch" cylindrical scaffolds from the larger printed squares. This same procedure was used to create samples for *in vivo* studies, although the offset between layers was not utilized and 400 μm spacing between fibers was used. Tensile specimens were 3D-printed using 200 μm diameter tips and 180 μm spacing between fibers (to ensure enough overlap to create a solid specimen). Each specimen was six printed layers thick with all layers created through fiber deposition oriented along the length of the specimen. Compression specimens were printed from 200 μm diameter tips as 1 cm diameter, 1 cm tall cylinders with 0.5 mm spacing between fibers and 0−90° orientation. Specimens for electrical testing were directly printed onto glass slides or PEN sheets. All electrical specimens comprised a single layer and a continuous fiber of known length.

Fiber Diameter and Flake Alignment Analysis. Consistency of fiber diameter detailed in Figure 2g was determined by first freeze fracturing a 40 layer, 0−90°, 2 cm diameter 60 vol % graphene scaffold printed with a 100 μm tip. The resulting cross section was examined using SEM, and the diameter of three fibers in every third layer was measured using ImageJ. Averages and standard deviations within each layer were determined as well as the average and total standard deviation of all fibers measured. Alignment of graphene flakes was assessed by end-on cross sectional scanning electron microscopy of graphene fibers, extruded from a 200 μm diameter tip, from within the center of a 1 cm diameter, 40 layer thick scaffold. Flake orientation in the plane of the image was measured along the major axis of the flake using ImageJ analysis software, with the angle measured with respect to the horizontal. The histogram in Figure 2e represents the result for 122 individual flakes.

Mechanical Testing. PLG, 3DG, and related graphene−PLG composites were 3D-printed into 20 mm gauge length tensile specimens from respective inks. Cast tensile specimens were prepared by casting 60 vol % graphene ink into Teflon-coated dishes and stamping out using a 20 mm gauge length tensile specimen stamp. All tensile and compression tests were performed on an LF Plus mechanical tester (Lloyd Instruments). Tensile tests were performed under constant displacement of 2 mm/min. Compressive tests were performed at a compression rate of 2 mm/min on 40 layer, 1 cm diameter, 0−90° pattern 3DG cylinders 3D-printed using a 200 μm tip. All sample groups were measured in triplicate. Elastic modulus for each was determined using a 0.2% strain offset linear slope method.

Electrical Characterization. Unless otherwise specified, electrical measurements were carried out in air using a two-probe measurement setup with a Keithley source meter, with silver paste employed to contact the graphene fibers. Resistance measurements of single printed filaments were obtained along the direction of extrusion. Sample dimensions were measured using optical microscopy and stylus profilometry. In all cases, annealing was carried out in a tube furnace under air for 30 min at the specified temperature. The electrical resistance as a function of strain was monitored using a Fluke 179 digital multimeter as the printed graphene fiber was strained at a rate <0.01/s along its axis. Error bars in the measurements represent a standard deviation for 3−7 samples. Cyclic loading was performed with the PEN sheet attached to provide a well-defined and controlled strain distribution. The number of bending cycles was selected to illustrate the evolution of resistance with deformation. Because saturation in the electrical resistance is observed after ~20 cycles, going beyond 1000 cycles is unlikely to result in different behavior. All electrical properties were collected with dc measurements. It was verified that contact resistance effects were negligible using the two-probe measurement setup by varying the length of measured samples prior to more exhaustive electrical characterization.

***In Vitro* Cell Seeding.** Passage 2 hMSCs (Lonza, Walkersville) were expanded up to passage 5 using MSC basal medium and proliferation kit (Lonza, Walkersville) according to the vendor's instructions. iCell Neurons (Cellular Dynamics International, USA) were thawed and suspended in vendor-provided iCell Neuron medium. Prior to cell seeding, 3DG and PLG scaffolds were rinsed in 70% ethanol for 1 h followed by three 4 min rinses in sterile phosphate buffered saline (PBS). We have shown through previous work that this not only sterilizes the scaffolds but also removes residual solvents. Scaffolds were stored in PBS until cell seeding. Fifty thousand hMSCs were seeded into each scaffold *via* injection of 7 μL cell suspensions in a medium composed of 1× low glucose DMEM modified with 10% fetal bone serum, HEPES (4-(2-hydroxyethyl)-1-piperazine ethanesulfonic acid) buffer, L-glutamine, and 10 units antibiotic antimyotic (Invitrogen). Two hundred thousand iCell Neurons suspended in iCell Neuron medium (Cellular Dynamics International) were added to each scaffold in 10 μL aliquots. Five hundred microliters of respective media was added to each well 1 h after initial seeding. All cell-seeded samples were incubated at 37 °C in 5% CO_2. Materials and methods related to *in vitro* characterization, including imaging, DNA quantification, and gene expression *via* real-time polymerase chain reaction (PCR) analysis may be found in Supporting Information.

Subcutaneous Scaffold Implantation and *In Vivo* Sample Characterization. A single subcutaneous incision was made on the back of each female BALB/c mouse near the nape of the neck. A PLG scaffold was inserted under the skin and pushed to the left side of the mouse. A 3DG scaffold was inserted through the same incision and pushed to the right side of the back. Incisions were sutured closed using a single suture. Daily care for mice was administered by staff from Northwestern University's Center for Comparative Medicine. Mice were monitored daily by authors. Mice were sacrificed at 7 and 30 days (n = 2), at which point scaffolds and surrounding tissue were removed and prepared for further analysis. The surgical protocol followed NIH guidelines for the care and use of laboratory animals and was approved by Northwestern University's Animal Care and Use Committee (Chicago, IL, USA).

Nerve Conduit Implantation in Human Cadaver. A 2 cm long section was preemptively cut from the as-printed 12 cm long 3DG nerve conduit cylinder (Figure 7f) using a scalpel. The dorsal branch of the ulnar nerve in an unfixed human cadaver was exposed, and the 3DG nerve conduit was cut longitudinally and wrapped around the intact nerve. The 3DG nerve conduit was stitched to the epineurium using a 7-0 prolene suture. Excess 3DG conduit length was then intraoperatively trimmed. Finally, the nerve was transected, and two additional sutures were used to attached the nerve to the 3DG nerve conduit.

Statistical Analyses. Tensile specimens were tested with n = 4. Sample sizes for electrical tests ranged between 3 and 7. Two tail t tests were utilized to determine significance between groups with a confidence level of 0.05.

Conflict of Interest: The authors declare no competing financial interest.

Acknowledgment. The authors acknowledge the support and the use of the following facilities: Northwestern University Cell Imaging Facility supported by NCI CCSG P30 CA060553 awarded to the Robert H. Lurie Comprehensive Cancer Center; EPIC facility (NU*ANCE* Center − Northwestern University) supported by NSF DMR-1121262 and EEC-0118025|003; Northwestern University Mouse Histology and Phenotyping Laboratory and Cancer Center supported by NCI CA060553; and the Equipment Core Facilities at the Simpson Querrey Institute for BioNanotechnology at Northwestern University developed by

support from The U.S. Army Research Office, the U.S. Army Medical Research and Material Command, and Northwestern University. The authors acknowledge Phillip L. Lewis for his help with cell seeding onto 3DG, Karl W. Putz for helpful discussions, Seth Lee for designing and providing the neurogenic primers and associated specific DNA annealing and replication protocols, Wei Xu for immunohistochemical sample preparation, Soleil Leilabadi for assistance with gross histological organ imaging and analyses, and Cellular Dynamics International (Madison, WI) for graciously providing the iCell Neurons. This research was also supported by Northwestern University's International Institute for Nanotechnology (NU# SP0030341), Northwestern University's McCormick Research Catalyst Award and the Office of Naval Research MURI Program (N00014-11-1-0690). A.E.J. and E.B.S. were supported in part by the Department of Defense (DoD) through the National Defense Science and Engineering Graduate (NDSEG) Fellowship Program.

Supporting Information Available: Additional supplementary figures, tables, and videos. This material is available free of charge *via* the Internet at http://pubs.acs.org.

REFERENCES AND NOTES

1. Novoselov, K. S.; Geim, A. K.; Morozov, S. V.; Jiang, D.; Zhang, Y.; Dubonos, S. V.; Grigorieva, I. V.; Firsov, A. A. Electric field effect in atomically thin carbon films. *Science* **2004**, *306*, 666–669.
2. Castro Neto, A. H.; Guinea, F.; Peres, N. M. R.; Novoselov, K. S.; Geim, A. K. The electronic properties of graphene. *Rev. Mod. Phys.* **2009**, *81*, 109–162.
3. Lee, C.; Wei, X. D.; Kysar, J. W.; Hone, J. Measurement of the elastic properties and intrinsic strength of monolayer graphene. *Science* **2008**, *321*, 385–388.
4. Balandin, A. A.; Ghosh, S.; Bao, W. Z.; Calizo, I.; Teweldebrhan, D.; Miao, F.; Lau, C. N. Superior thermal conductivity of single-layer graphene. *Nano Lett.* **2008**, *8*, 902–907.
5. Schwierz, F. Graphene transistors. *Nat. Nanotechnol.* **2010**, *5*, 487–496.
6. Stoller, M. D.; Park, S. J.; Zhu, Y. W.; An, J. H.; Ruoff, R. S. Graphene-based ultracapacitors. *Nano Lett.* **2008**, *8*, 3498–3502.
7. Sinar, D.; Knopf, G. K.; Nikumb, S. Graphene-based inkjet printing of flexible bioelectronic circuits and sensors. *SPIE* **2013**, 861204.
8. Shao, Y.; Wang, J.; Wu, H.; Liu, J.; Aksay, I. A.; Lin, Y. Graphene based electrochemical sensors and biosensors: a review. *Electroanalysis* **2010**, *22*, 1027–1036.
9. Shen, H.; Zhang, L. M.; Liu, M.; Zhang, Z. J. Biomedical applications of graphene. *Theranostics* **2012**, *2*, 283–294.
10. Zhang, Y.; Nayak, T. R.; Hong, H.; Cai, W. B. Graphene: a versatile nanoplatform for biomedical applications. *Nanoscale* **2012**, *4*, 3833–3842.
11. Hu, X. H.; Li, D.; Tan, H. P.; Pan, C. B.; Chen, X. X. Injectable graphene oxide/graphene composite supramolecular hydrogel for delivery of anti-cancer drugs. *J. Macromol. Sci., Part A: Pure Appl. Chem.* **2014**, *51*, 378–384.
12. Chen, G. Y.; Pang, D. W. P.; Hwang, S. M.; Tuan, H. Y.; Hu, Y. C. A graphene-based platform for induced pluripotent stem cells culture and differentiation. *Biomaterials* **2012**, *33*, 418–427.
13. Wujcik, E. K.; Monty, C. N. Nanotechnology for implantable sensors: carbon nanotubes and graphene in medicine. *Wiley Interdiscip. Rev.: Nanomed. Nanobiotechnol.* **2013**, *5*, 233–249.
14. Yao, J.; Sun, Y.; Yang, M.; Duan, Y. X. Chemistry, physics and biology of graphene-based nanomaterials: new horizons for sensing, imaging and medicine. *J. Mater. Chem.* **2012**, *22*, 14313–14329.
15. Fraczek-Szczypta, A. Carbon nanomaterials for nerve tissue stimulation and regeneration. *Mater. Sci. Eng., C* **2014**, *34*, 35–49.
16. Lee, S. K.; Kim, H.; Shim, B. S. Graphene: an emerging material for biological tissue engineering. *Carbon Lett.* **2013**, *14*, 63–75.
17. Bitounis, D.; Ali-Boucetta, H.; Hong, B. H.; Min, D.-H.; Kostarelos, K. Prospects and challenges of graphene in biomedical applications. *Adv. Mater.* **2013**, *25*, 2258–2268.
18. Bressan, E.; Ferroni, L.; Gardin, C.; Sbricoli, L.; Gobbato, L.; Ludovichetti, F. S.; Tocco, I.; Carraro, A.; Piattelli, A.; Zavan, B. Graphene based scaffolds effects on stem cells commitment. *J. Transl. Med.* **2014**, *12*, 296.
19. Torrisi, F.; Hasan, T.; Wu, W. P.; Sun, Z. P.; Lombardo, A.; Kulmala, T. S.; Hsieh, G. W.; Jung, S. J.; Bonaccorso, F.; Paul, P. J.; Chu, D. P.; Ferrari, A. C. Inkjet-printed graphene electronics. *ACS Nano* **2012**, *6*, 2992–3006.
20. Li, N.; Zhang, Q.; Gao, S.; Song, Q.; Huang, R.; Wang, L.; Liu, L.; Dai, J.; Tang, M.; Cheng, G. Three-dimensional graphene foam as a biocompatible and conductive scaffold for neural stem cells. *Sci. Rep.* **2013**, *3*, 1604.
21. Secor, E. B.; Prabhumirashi, P. L.; Puntambekar, K.; Geier, M. L.; Hersam, M. C. Inkjet printing of high conductivity, flexible graphene patterns. *J. Phys. Chem. Lett.* **2013**, *4*, 1347–1351.
22. Secor, E. B.; Lim, S.; Zhang, H.; Frisbie, C. D.; Francis, L. F.; Hersam, M. C. Gravure printing of graphene for large-area flexible electronics. *Adv. Mater.* **2014**, *26*, 4533–4538.
23. Noel, A.; Faucheu, J.; Rieu, M.; Viricelle, J. P.; Bourgeat-Lami, E. Tunable architecture for flexible and highly conductive graphene-polymer composites. *Compos. Sci. Technol.* **2014**, *95*, 82–88.
24. Sun, G.; An, J.; Chua, C. K.; Pang, H.; Zhang, J.; Chen, P. Layer-by-layer printing of laminated graphene-based interdigitated microelectrodes for flexible planar micro-supercapacitors. *Electrochem. Commun.* **2015**, *51*, 33–36.
25. Xu, Y. X.; Sheng, K. X.; Li, C.; Shi, G. Q. Self-assembled graphene hydrogel via a one-step hydrothermal Process. *ACS Nano* **2010**, *4*, 4324–4330.
26. Tolle, F. J.; Fabritius, M.; Mulhaupt, R. Emulsifier-free graphene dispersions with high graphene content for printed electronics and freestanding graphene films. *Adv. Funct. Mater.* **2012**, *22*, 1136–1144.
27. Nathan-Walleser, T.; Lazar, I.-M.; Fabritius, M.; Tölle, F. J.; Xia, Q.; Bruchmann, B.; Venkataraman, S. S.; Schwab, M. G.; Mülhaupt, R. 3D Micro-extrusion of graphene-based active electrodes: towards high-rate AC line filtering performance electrochemical capacitors. *Adv. Funct. Mater.* **2014**, *24*, 4706–4716.
28. Sun, K.; Wei, T. S.; Ahn, B. Y.; Seo, J. Y.; Dillon, S. J.; Lewis, J. A. 3D Printing of interdigitated Li-ion microbattery architectures. *Adv. Mater.* **2013**, *25*, 4539–4543.
29. Seol, Y. J.; Kang, H. W.; Lee, S. J.; Atala, A.; Yoo, J. J. Bioprinting technology and its applications. *Eur. J. Cardiothorac. Surg.* **2014**, *46* , 342–348.
30. Leigh, S. J.; Bradley, R. J.; Purssell, C. P.; Billson, D. R.; Hutchins, D. A. A Simple, low-cost conductive composite material for 3D printing of electronic sensors. *PLoS One* **2012**, *7*, e49365.
31. Muth, J. T.; Vogt, D. M.; Truby, R. L.; Mengüç, Y.; Kolesky, D. B.; Wood, R. J.; Lewis, J. A. Embedded 3D printing of strain sensors within highly stretchable elastomers. *Adv. Mater.* **2014**, *26*, 6307–6312.
32. Ahn, B. Y.; Shoji, D.; Hansen, C. J.; Hong, E.; Dunand, D. C.; Lewis, J. A. Printed origami structures. *Adv. Mater.* **2010**, *22*, 2251.
33. Xu, Z.; Zhang, Y.; Li, P.; Gao, C. Strong, conductive, lightweight, neat graphene aerogel fibers with aligned pores. *ACS Nano* **2012**, *6*, 7103–7113.
34. Mogharabi, M.; Abdollahi, M.; Faramarzi, M. A. Safety concerns to application of graphene compounds in pharmacy and medicine. *Daru* **2014**, *22*, 3.
35. Cancino, J.; Marangoni, V. S.; Zucolotto, V. Nanotechnology in medicine: concepts and concerns. *Quim. Nova* **2014**, *37*, 521–526.
36. Anderson, J. M.; Shive, M. S. Biodegradation and biocompatibility of PLA and PLGA microspheres. *Adv. Drug Delivery Rev.* **1997**, *28*, 5–24.
37. Elias, R. A. I.; Maikos, J. T.; Shreiber, D. I. Mechanical properties of dura mater from the rat brain and spinal cord. *J. Neurotrauma* **2008**, *25*, 38.

38. Ozawa, H.; Matsumoto, T.; Ohashi, T.; Sato, M.; Kokubun, S. Mechanical properties and function of the spinal pia mater. *J. Neurosurg. Spine* **2004**, *1*, 122–127.
39. Akhtar, R.; Sherratt, M. J.; Cruickshank, J. K.; Derby, B. Characterizing the elastic properties of tissues. *Mater. Today* **2011**, *14*, 96–105.
40. Jiang, Y.; Jahagirdar, B. N.; Reinhardt, R. L.; Schwartz, R. E.; Keene, C. D.; Ortiz-Gonzalez, X. R.; Reyes, M.; Lenvik, T.; Lund, T.; Blackstad, M.; Du, J.; Aldrich, S.; Lisberg, A.; Low, W. C.; Largaespada, D. A.; Verfaillie, C. M. Pluripotency of mesenchymal stem cells derived from adult marrow. *Nature* **2002**, *418*, 41–49.
41. Cole, J. S.; Messing, A.; Trojanowski, J. Q.; Lee, V. M. Y. Modulation of axon diameter and neurofilaments by hypomyelinating schwann-cells in transgeneic mice. *J. Neurosci.* **1994**, *14*, 6956–6966.
42. Bressan, E.; Ferroni, L.; Gardin, C.; Sbricoli, L.; Gobbato, L.; Ludovichetti, F. S.; Tocco, I.; Carraro, A.; Piattelli, A.; Zavan, B. Graphene based scaffolds effects on stem cells commitment. *J. Transl. Med.* **2014**, *12*, 296.
43. Park, S. Y.; Park, J.; Sim, S. H.; Sung, M. G.; Kim, K. S.; Hong, B. H.; Hong, S. Enhanced differentiation of human neural stem cells into neurons on graphene. *Adv. Mater.* **2011**, *23*, H263–H267.
44. Tang, M.; Song, Q.; Li, N.; Jiang, Z.; Huang, R.; Cheng, G. Enhancement of electrical signaling in neural networks on graphene films. *Biomaterials* **2013**, *34*, 6402–6411.
45. Wang, Y.; Lee, W. C.; Manga, K. K.; Ang, P. K.; Lu, J.; Liu, Y. P.; Lim, C. T.; Loh, K. P. Fluorinated graphene for promoting neuro-induction of stem cells. *Adv. Mater.* **2012**, *24*, 4285–4290.
46. De Laporte, L.; Yang, Y.; Zelivyanskaya, M. L.; Cummings, B. J.; Anderson, A. J.; Shea, L. D. Plasmid releasing multiple channel bridges for transgene expression after spinal cord injury. *Mol. Ther.* **2009**, *17*, 318–326.
47. Whittlesey, K. J.; Shea, L. D. Nerve growth factor expression by PLG-mediated lipofection. *Biomaterials* **2006**, *27*, 2477–2486.
48. Marquardt, L. M.; Sakiyama-Elbert, S. E. Engineering peripheral nerve repair. *Curr. Opin. Biotechnol.* **2013**, *24*, 887–892.